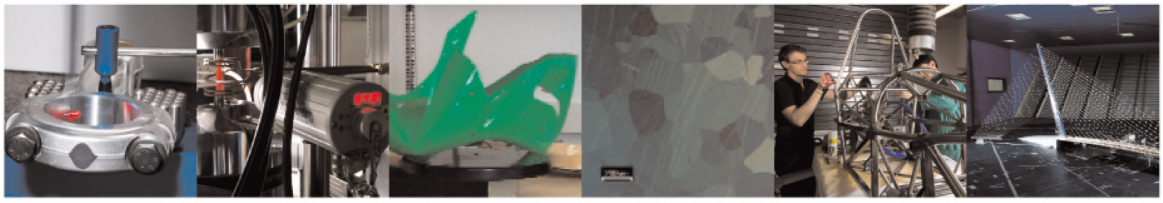

Additive manufacturing of lead-free KNN by binder jetting

Mariani Marco;Beltrami Ruben;Migliori Emanuele;Cangini Laura;Mercadelli Elisa;Baldisserri Carlo;Galassi Carmen;Lecis Nora

Additive manufacturing of lead-free KNN by binder jetting

Marco Mariani[a], Ruben Beltrami[a], Emanuele Migliori[a], Laura Cangini[b], Elisa Mercadelli[b]*, Carlo Baldisserri[b], Carmen Galassi[a,b], Nora Lecis[a]

[a] Department of Mechanical Engineering, Politecnico di Milano, Milano 20156, Italy

[b] CNR-ISTEC, Istituto di Scienza e Tecnologia dei Materiali Ceramici, Faenza 48018, Italy

*Corresponding author: elisa.mercadelli@istec.cnr.it

Abstract

Additive manufacturing of lead-free piezoceramics is of great interest, given the large request of application-oriented designs with optimal performances and reduced material consumption. Binder Jetting (BJ) is an additive manufacturing technique potentially suited to the production of ceramic components, however the number of feasibility studies on BJ of piezoceramics is extremely limited and totally lacking in the case of sodium-potassium niobate (KNN).

In this work, as-synthesised powders are employed in the BJ 3D printing process. Microstructural properties, such as porosity, grain size distributions, and phase composition are studied by SEM, XRD and MIP (Mercury Intrusion Porosimetry) and compared to die-pressed pellets. Analyses reveal considerable residual porosity (~40%) regardless of the printing parameters, with a weak preferential orientation parallel to the printing plane. The piezoelectric characterization demonstrates an outstanding d_{33} value of 80-90 pC N^{-1}. Finally, Figures of Merits for the employment as porous piezoceramics in the direct mode are presented.

Keywords: Binder jetting; Additive Manufacturing; Piezoceramic; Binder saturation; Porosity.

1. Introduction

In the last decade, additive manufacturing (AM) has been increasingly adopted due to some of its features, such as design freedom and speed of production, which give a competitive advantage over conventional manufacturing. However, the commercialisation of such processes and products has regarded mainly metallic items obtained by direct AM processes (e.g., Laser- and Electron Beam- Powder Bed Fusion (L-PBF and EB-PBF), Direct Energy Deposition (DED)), whereas ceramic materials are still facing considerable issues that have left their shaping by additive manufacturing techniques at a preliminary stage [1,2]. Nonetheless, AM would find great opportunities for application in this class of material, in particular when functional ceramics are considered, since they usually have to satisfy less stringent mechanical requirements compared to metals or structural ceramics and could benefit greatly from customised solutions [3]. In this scenario, indirect AM techniques such as Fused Deposition Modelling (FDM), Stereolithography (SLA), and Binder Jetting (BJ), are gathering attention because they allow achieving the shaping of components without the need of high temperatures, and to reach high densification by sintering with treatments and equipment like those employed by the press-and-sinter route.

Piezoceramics are employed widely in industries as electronics, healthcare, power generation. In these cases, AM would allow achieving improved performances and reduce material waste. Moreover, the possibility to design and manufacture complex structures and novel architectures in a wide size-range scale, would pave the way towards new studies and application fields such as integrated electronics, tissue engineering and other advanced intelligent devices [4]. However, issues as sensitivity to processing conditions and absence of raw materials tailored for this type of techniques have so far prevented their development

[5]. In addition, the EU ban on the use of lead-zirconium titanate (PZT) has further limited the availability of resources that could fit these processes and grant acceptable performance [6].

So far, most studies have focused on the use of barium titanate $BaTiO_3$ (BT) for SLA. Both have features that limit the field of potential applications. BT is a soft piezoceramic, which makes it ideal for sensors but unstable at high temperature or when subject to high mechanical loads and high voltages. On the other hand, SLA offers good resolution and fast prototyping. However, the preparation of stable suspensions with photosensitive polymers can be challenging, and there can be significant waste of feedstock material at the end of the process. In this work, lead-free sodium-potassium niobate $(K_{0.5}Na_{0.5})NbO_3$ (KNN) was singled out as the material of choice due to its hard piezoelectricity, which makes it ideal for energy conversion applications, and BJ was explored as a possible alternative route for its cold consolidation. To the authors' knowledge, there is no previous literature on this combination of material and process. KNN has been previously produced by SLA [7] and BJ has been employed by Sufiiarov et al., Chavez et al., and Gaytan et al. to manufacture BT [8–10].

Powders employed in binder jetting should typically have optimal flowability, determined by both their (spherical) shape and proper particle size distribution (wide unimodal or bimodal), to pack properly [11–13]. In our study, the powder was not optimised for additive manufacturing use; however, it yielded optimal results when cold consolidated by die pressing. Therefore, this study is aimed at assessing the feasibility of combining binder jetting with ready-to-use powder to produce KNN components with comparable performance to that of traditionally processed ones.

2. Materials and Methods

2.1. Materials

KNN powders were synthesised through a mechanochemical-activation-assisted solid-state reaction method [14]. Na_2CO_3 (Merck, 99.5%), K_2CO_3 (Merck, 99%) and Nb_2O_5 (Aldrich, 99.99%) were dried at 80 °C for 24 h, weighed and planetary milled in a zirconia jar with a Fritsch Planetary Mill (PULVERISETTE 6). Distilled water was used as dispersing medium (2:1 water/powders weight ratio) while yttria-stabilized zirconia balls (2 mm diameter) were used ad milling media, setting 6:1 the balls-to-powder weight ratio. The milling was set to last 100 min with a rotation speed of 600 rpm. The as-milled slurry was freeze-dried, and the resulting powder sieved and calcined at 700 °C for 9 h. The as-calcined powder was planetary-milled at 400 rpm for 120 min and finally freeze-dried and sieved. The as-obtained powder was not subjected to any granulation processes before BJ.

2.2. Printing and Post-Processing

Small (diameter = 10 mm, thickness = 1 mm) and larger (diameter = 20 mm, thickness = 2 mm) disks were produced via BJ using an Innovent+ 3D printer by ExOne Inc. Prior to printing, the powder was dried at 120 °C for 24 hours to remove residual humidity and obtain a suitable flowability of the material through the hopper. The organic binder used for BJ was the commercially available AquaFuse® (previously known as BA005), provided by ExOne Inc.

Three different binder saturations (BS) were tested for the smaller geometries: 75%, 90% and 120%. These values correspond to the ratio between the volume of the deposited binder and that of the powder bed porosity. All larger disks were, instead, printed at 90% binder saturation. Layer thickness (LT) was kept constant at 50 µm to ensure good geometrical resolution and minimise the risk of macropores formation, usually associated with the spreading of larger layers with poorly flowing powders [15].

The powder bed was cured at 180 °C for 6 hours in air to obtain the polymerisation of the monomer dissolved in the binder and the evaporation of the residual solvents. The sintering

process was performed in a sealed alumina crucible at 1130 °C for 2 hours with a 2.5 °C min^{-1} heating rate, in the presence of KNN pack powder with 2 wt.% alkali excess. The disks were densified by single and double sintering, where the latter consisted in densifying the samples through two consecutive sintering cycles separated by cooling of the specimens to room temperature.

Specimens obtained by different combinations of printing parameters, size, and sintering conditions are referred to as explained in Table 1.

Additionally, fully dense samples were produced through press-and-sinter to compare the properties of components obtained by additive and conventional manufacturing. These were densified for 2 hours at 1130 °C with a heating rate of 2.5 °C min^{-1} in presence of pack powder, exactly as for the mono-sintered components.

Table 1 Nomenclature of the specimens according to binder saturation (BS 75, 90, 120), the geometry size (S= small, L= large), and number of sintering cycles (1,2) performed.

Sample name	BS / %	Size	Number of sintering cycles
75S1	75	Small	1
90S1	90	Small	1
120S1	120	Small	1
90L2	90	Large	2

2.3. Characterisations

The KNN powder morphology was analysed by field emission-scanning electron microscopy (FE-SEM) in a ZEISS SIGMA 500 FE-SEM unit, while the particles size distribution was analysed by optical granulometry (ASTM E2651-19) using a Malvern Morphology 4 unit (resolution = 150 nm), which allowed calculating the cumulative and relative frequency curves of the number-based size distribution. An analysis of powder

flowability was obtained with a FT4 Powder Rheometer 2 that measured the values of apparent density (ρ_{app}), corresponding to the as-poured material (ASTM B417-18), and tapped density (ρ_{tap}) after compaction (ASTM B527-20). The Hausner (H) index, defined as follows in Eq. 1, gave an estimate of the feedstock flowability:

$$H = \rho_{tap} / \rho_{app} \quad (1)$$

X-ray diffraction (XRD) analyses on both the starting powder and the sintered samples were performed over the $20° \leq 2\theta \leq 80°$ range (step size 0.02°) at a scanning rate of 1° min^{-1} with Cu-Kα radiation (λ = 1.5406 Å) in a Smartlab II Rigaku diffractometer. For XRD measurements the sintered samples were prepared by grinding, sieving, annealing at 700 °C for 30 minutes, and an additional final sieving. The $K_{0.5}Na_{0.5}NbO_3$ phase was identified by the structure file COD DB #2300499 [16]. Rietveld refinements of the diffraction patterns were carried out using GSAS-II© (General Structure Analysis System) software.

The green and sintered densities of both small and large sized samples were evaluated by the geometrical method. Relative density values were calculated with reference to the theoretical density of 4.50 g cm^{-3}.

Both fracture surfaces and polished sections of the sintered samples were investigated by FE-SEM. Grain size distribution of the ceramics was determined by machine learning segmentation employing the trainable WEKA plugin of ImageJ on the SEM micrograph of polished cross-section surface. The overall pore volume and the pore size distribution of the sintered samples were calculated by Mercury Intrusion Porosimetry (MIP). The analysis was performed in an Autopore V9600 unit built by the Micrometrics Instrument Corporation (US). The Washburn equation (Eq. (1)) was employed to calculate the pore diameters from the infiltration pressure at the different stages of the process:

$$d = - (4 \gamma \cos\theta) / P \quad (1)$$

where d is the diameter of the intruded porosity, γ is the mercury surface tension (485.5 mN m^{-1} at room temperature), θ is the contact angle between mercury and the porosity internal surface (for Hg-GDM the value recorded is 130°) and P is the external pressure applied to the mercury by the instrument.

Silver-electroded samples were dielectrically, piezoelectrically and mechanically characterised after the poling process (3 kV mm^{-1} at 120 °C for 40 min), by acquiring their room-temperature piezoresonance spectra with an HP 4194A (Hewlett Packard, US) impedance analyser, detecting resonance and antiresonance frequencies over the 100 Hz–40 MHz range. Room-temperature capacitance and loss tangent were measured at 1 kHz using the same instrument. Dielectric, piezoelectric, and mechanical parameters were calculated according to the 1986 ASTM Standard on Piezoelectricity. d_{33} piezoelectric charge coefficient values were separately measured using a Sinocera S 5865 d_{33}-meter calibrated with a standard sample provided by the manufacturer. For the thicker 90L2 samples, the d_{33} was calculated both along the parallel orientation and the perpendicular orientation with respect to the layer deposition direction (Figure 1) to evaluate the possible effect of the oriented porosity.

For clarity, _PAR and _PER are added to the samples name when necessary to distinguish the properties measured in the parallel and perpendicular direction, respectively.

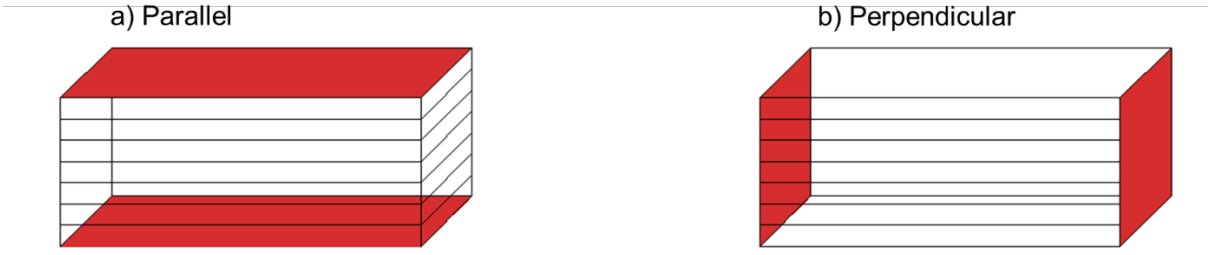

Figure 1 Schematic representation of the d_{33} measurement direction with respect to the layer deposition orientation. Red areas represent the electrodes.

3. Results and Discussion

3.1 Morphological and microstructural characterization

3.1.1. KNN Powder

SEM image in Figure 2A shows that powder particles have an irregular shape and their size covers an extended range. Indeed, ultra-fine sub-micron size particles were detected (Figure 2C); there are agglomerates whose dimension falls within the 1 to 10 μm range; finally, a few larger platelets-like fragments are also present. The finer fraction either form irregular agglomerates or tends to stick to the flat surface of the larger particles (Figure 2B).

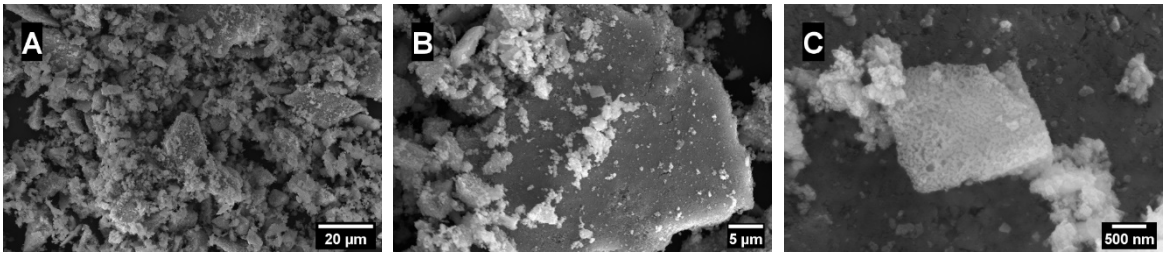

Figure 2 SEM images of the KNN powder at different magnification levels.

Granulometric measurements in Figure 3 confirmed the observations made by SEM analyses of particles size. As summarised in Table 2, most particles are in the 100 – 500 nm range, while agglomerates and platelets size is above 1.5 μm. It should be noted that, during sample preparation for granulometry, particles dispersion occurs by compressed air blowing, which may disaggregate some larger particles, thus increasing the count of the finer fraction.

The wide particle size distribution may improve the packing of the powder, with smaller granules filling the voids between the larger ones, and the fine fraction might be helpful in promoting the sintering mechanisms during post-printing treatments [17–19]. However, it

should also be considered that small dimensions in combination with irregular shape could severely impair the flowability of the material [20,21].

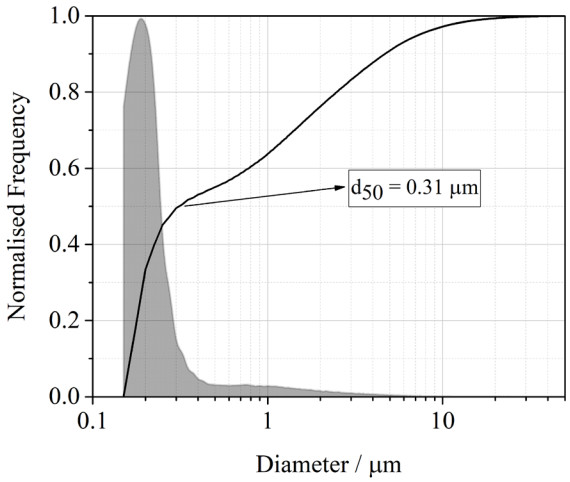

Figure 3 Cumulative (solid line) and relative frequency (grey area) distribution curves of KNN powder.

The Hausner ratio (H) is much higher than 1.2, the threshold value for a properly flowing powder (Table 2) [22]. Factors influencing flowability are low density of the powder, its hygroscopicity, and its irregular shape, which favour the formation of low-density aggregates due to electrostatic interactions, capillarity, and mechanical interlocking [22,23]. In this case, the only improvement could be obtained by completely drying the powder before printing, as described in Paragraph 2.2, to remove residual humidity.

In addition, the intrinsic porosity of the powder is particularly relevant, given that the relative density is extremely low even after compaction, as measured by tapped density (Table 2).

Table 2 Granulometric (particle size (μm) distribution values) and rheometric (apparent density (%), tapped density (%) and Hausner ratio) values obtained from measurements on KNN powder.

Granulometry	**Rheometry**

d_{10} / µm	d_{50} / µm	d_{90} / µm	$\rho_{app}^{(I)}$ / %	$\rho_{tap}^{(I)}$ / %	H
0.15	0.31	4.69	13.8 ± 1.3	24.6 ± 1.5	1.78 ± 0.1

(I) expressed as a percentage of solid state KNN bulk density (4.50 g cm^{-3}).

3.1.2. Green Body

The printing procedure seems to be slightly beneficial to the packing of the powder. Indeed, all the printed samples featured a relative green density higher than 30%, as can be seen in Figure 8, while the tapped density was only 24.6 ± 1.5 % (Table 2). This might be explained by two factors: first, the binder partially fills the voids of the powder bed (depending on binder saturation), thus contributing its own weight to that of the sample; second, the layer-by-layer deposition and the spreading action of the roller on a limited amount of material may favour the rearrangement of the particles, which could prevent excessive formation of voids in the powder bed [21,23]. The contribution from the binder weight seems to be confirmed by the correlation between binder saturation and green density.

3.1.3. Sintered samples

XRD analyses were performed on mono-sintered and bi-sintered samples (Figure 4). The XRD spectra are compared to the one registered for the KNN powder. The results highlight that - both in powders and sintered samples - only $K_{0.5}N_{0.5}NbO_3$ peaks are present, and that no secondary phases are formed during the selected thermal treatments (calcination/sintering). In particular, the XRD spectra and the calculated unit-cell parameters of the sintered samples (Table 3) demonstrate that neither structural changes nor secondary phases occur using different binder saturations (75S1, 90S1, and 120S1) or after a second

sintering treatment (90L2). While, the broad peaks of the powder pattern once again emphasize the role of the finer particles fraction [24].

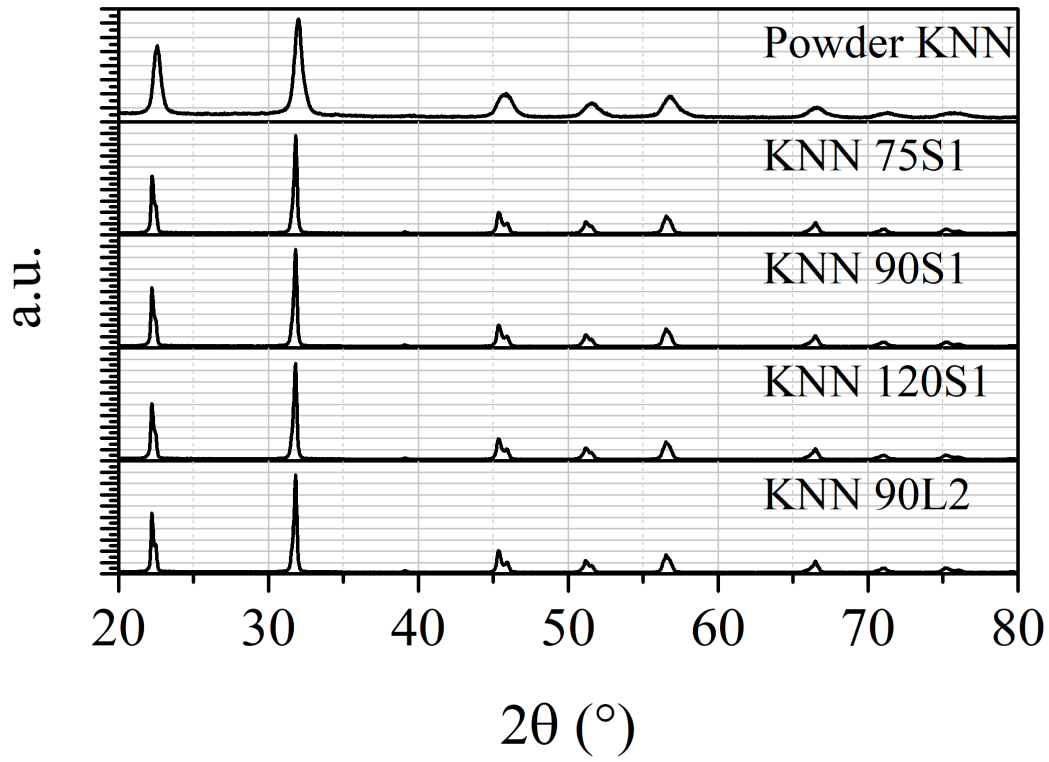

Figure 4 XRD spectra of the KNN powder, mono-sintered samples (75S1, 90S1, 120S1) and bi-sintered sample (90L2).

Table 3 Refinement agreement factors and unit-cell parameters for the sintered KNN samples.

Sample	Refin. agreement factors			$K_{0.5}Na_{0.5}NbO_3$ phase				
	Rw %	χ^2_r	GOF	R_f^2 %	a	b Å	c	Cell volume Å^3
KNN 75S1	7.9	3.57	1.89	2.81	3.956	5.636	5.665	126.316
KNN 90S1	7.74	3.41	1.85	3.09	3.956	5.637	5.665	126.325
KNN 120S1	7.71	3.41	1.85	2.72	3.956	5.636	5.665	126.314
KNN 90L2	7.8	3.38	1.84	3.15	3.955	5.638	5.665	126.324

After a single sintering cycle, all samples feature a reduced shrinkage and significant differences are not observed between different binder saturations. However, it should be noted that the limited size and some distortion of the disk planar surface hindered the acquisition of very precise geometrical measurements. The density values obtained corresponded to 29.5 ± 0.5 %, 30.3 ± 0.4 %, and 31.8 ± 1.1 % for the 75S1, 90S1 and 120S1, respectively. These densities are slightly lower than those of the green samples, which is likely due to the saturation of the binder: at the green stage, the binder own weight gives a sizable contribution to that of the samples; however, during the sintering process, the polymer is completely pyrolyzed and removed, thus generating additional open porosity inside the microstructure that is not compensated for during sintering, which likely featured mainly surface diffusion mechanisms that did not promote densification [25,26]. In addition, an excessive amount of binder might lead to the risk of overfilling the voids, thus pushing the particles apart and increasing the distance among them [13,27].

SEM micrographs of cross-section surfaces in Figure 5 confirm the presence of significant internal porosity. It is possible to distinguish three types of voids in the microstructure:

- inter-layer cracks and fractures of varying length, up to 300 μm in some cases (Figure 5A);
- macropores placed along the layer surfaces, likely formed in between the single binder droplets during the printing phase (1 - 15 μm) (Figure 5B);
- micropores within the densified regions resulting from the incomplete closure of the dihedral pores in between KNN grains (Figure 5C).

The porosity distribution in the sintered samples is confirmed by results of MIP performed on the 90S1 sample, shown in Figure 6A. In addition, Figure 5A shows that the macroporosity is preferentially oriented along the layer surface, which could result in an anisotropic

piezoelectric behaviour, particularly desired in porous piezoceramics working in the d_{33} mode.

Figure 5D shows the cross-section fracture surface of the 120S1 sample. While the samples 75S1 and 90S1 show similar microstructures, this material is characterised by an even wider network of macropores and large voids, which is likely the result of the excessive amount of binder. During printing, this overfilling mechanism might generate a local pressure on the powder bed and move the particles away from each other. After binder removal, this could result in a decrease of the number of contact points, which hinders the formation of necks and the diffusion mechanisms during sintering.

An important observation is that grain growth is quite limited: most grains have size below 1 μm, as can be seen from the frequency distributions in Figure 6B. Usually, domination of non-densifying mechanisms, being surface diffusion the most prevalent one, occurs at initial stage of KNN sintering causing rapid grain growth and poor densification [28,29]. In our case, however, the material featured only initial stage sintering without observation of abnormal grain growth since the final relative density is below 40%. This is likely due to the very small density of green bodies, which reduced the coordination number of the particles and increased the activation energies of both surface and volume diffusion mechanisms.

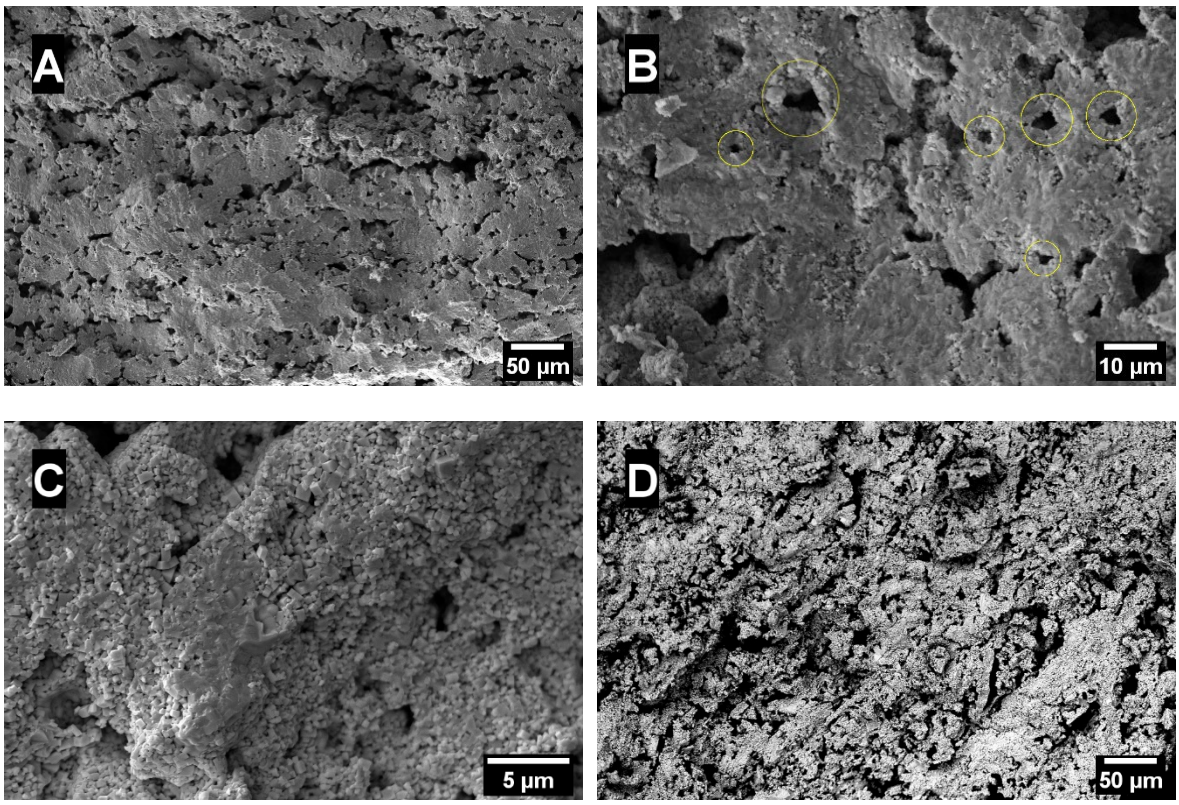

Figure 5 SEM micrographs of (A-B) the fracture surface of 90S1 sample, (C) the fracture surface of 75S1 sample and (D) the fracture surface of 120S1 sample.

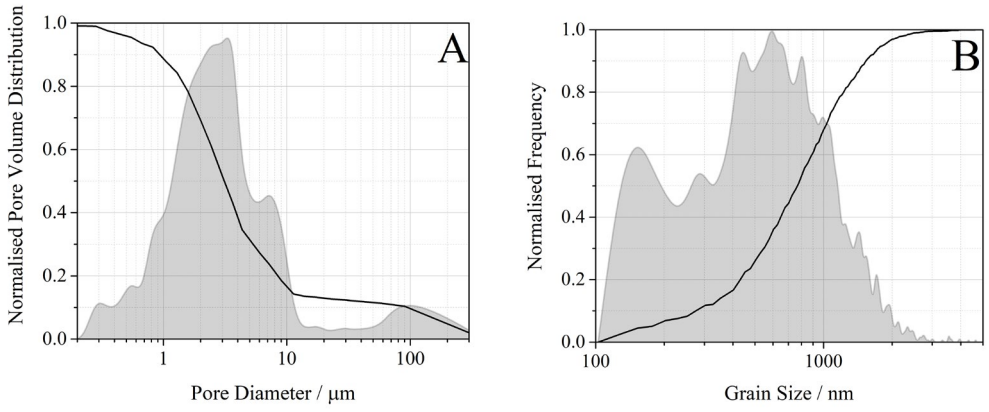

Figure 6 Microstructural features size: (A) Cumulative (solid line) and relative (grey area) porosity volume distribution obtained by MIP measurements on sample 90S1; (B) Cumulative (solid line) and relative (grey area) distributions of the grains size of the 90S1 sample.

To improve the final density of the KNN ceramics produced via BJ, a subsequent second sintering treatment at 1130 °C for 2h was employed for the 90L2 sample. However, it appears from the SEM images in Figures 7C and 7D that the additional thermal treatment promotes only partially the sintering mechanisms to enhance the densification. A final relative density of 56 % was in fact achieved after the second sintering step. This confirms again the poor sinterability of KNN-based systems due to the domination of non-densifying material transport mechanism, i.e. surface diffusion. The low activation energy of the latter induces the grain growth during the heating step, reducing the driving force for sintering during the main sintering stage [28].

It should also be noted that coarsening might be an issue, as larger grains tend to grow further generating microporosities at their boundary (Figures 7E and 7F). Volume diffusion mechanisms that are responsible for large densification gradients seem to not have occurred, which is coherent with the low final density. SEM micrographs on polished cross and longitudinal sections (Figure 7A and 7B) confirm that a well-oriented microstructure is absent, in particular in those regions of the solid where porosity is more relevant. It could be expected that an improvement of the final density could lead to a clearer distinction of the interlayer porosity, as observed in other studies [30–32]. On the one hand, this result highlights that exploiting BJ to achieve oriented microstructural development is more challenging than with other techniques like freeze-casting, where directional sintering is enhanced [33,34]. On the other hand, a more homogeneous internal structure allows a greater freedom of design since optimal performance is granted independently from the orientation considered.

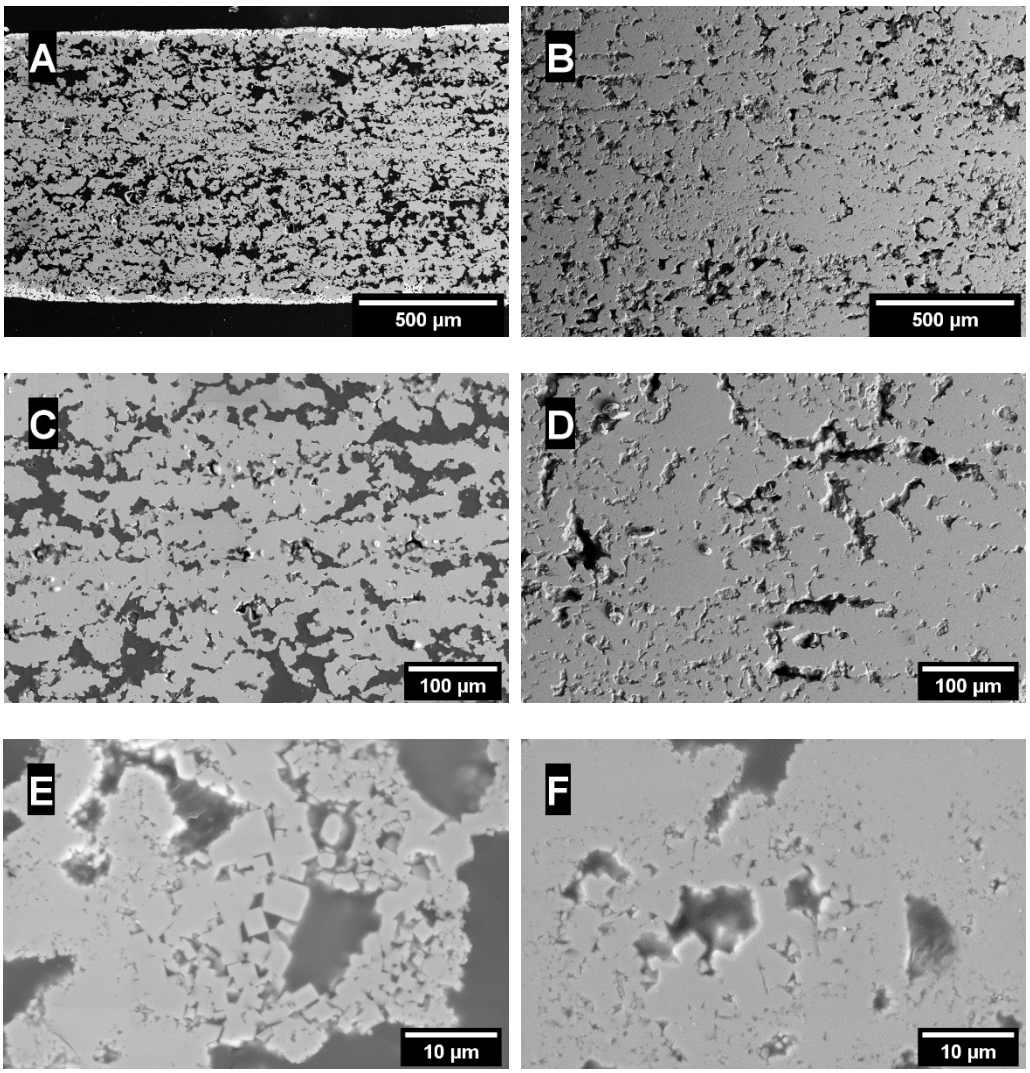

Figure 7 SEM micrographs of 90L2 bi-sintered components, specifically: (A, C, and E) polished cross section (perpendicular to the layer orientation) at different magnifications; (B, D, and F) polished longitudinal section (parallel to the layer orientation) at different magnifications.

3.2 Functional properties

d_{33} values measured for the three mono-sintered samples are promising if correlated with the extent of their densification (Fig. 8), except for the 120S1 sample, the response of the latter being 10 pC N^{-1} lower. Indeed, samples with higher density values (~ 92% relative density) obtained from the same powder by the pressing and sintering technique featured a d_{33} value of 105.6 ± 2.9 pC N^{-1}; the d_{33} value of the 90S1 sample is 70.5% with respect to that of the

92% relatively dense sample, which is larger than expected based on the ratio between the relative densities. 120S1 featured the lowest final d_{33} piezoelectric charge coefficient and the largest tan(δ) values (61 pC N^{-1} and 70%, respectively). The lack of an electrical path continuity or excessive tortuosity of the same could hinder the material polarization under an electric field, thus being responsible for the lower piezoelectric response of this sample.

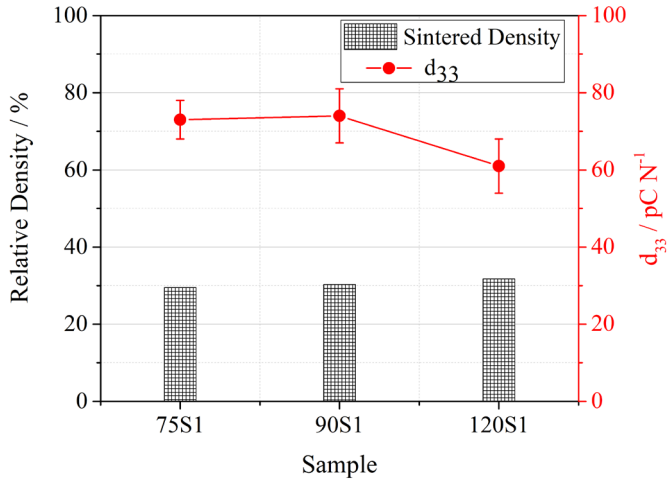

Figure 8 Sintered density and d_{33} values of the mono-sintered thin samples.

d_{33} measurements performed on the bi-sintered 90L2 sample (Table 4) show even higher piezoelectricity as compared to that of mono-sintered samples, with d_{33} values closer to those measured on dense samples. This could be attributed to the improved structural integrity of these samples compared to the thinner ones, likely due to the double sintering process and to the larger ratio between sample thickness and largest internal porosity or defects size (~100 μm), which may be relevant in case of production of complex geometries where thickness variations may be responsible for varying piezoelectric performance in different regions of the component. The first hypothesis is confirmed by the higher values of relative density that were achieved after the second sintering step, as can be seen in Table 4.

On the other hand, the effect of porosity orientation seems to be minimal. Values in Table 4 show a ~5 pC N^{-1} improvement of the d_{33} measured parallel to the layers deposition orientation that can be attributed to better structural continuity in this direction that increases the mechanical stiffness of the ceramic [9,35]. However, many contact surfaces between sintered layers are present, which hinders the unambiguous detection of differences in the piezoelectric behaviours of the 90L2_PER and 90L2_PAR samples.

Table 4 d_{33} values measured for the 90S1 (mono-sintered), 90L2_PER and 90L2_PAR (bi-sintered) samples.

	90S1	**90L2_PAR**	**90L2_PER**	**DENSE**
d_{33} / pC N^{-1}	74.1 ± 7.0	84.8 ± 9.2	89.9 ± 3.8	105.6 ± 2.9
Q_m	22.3	27.4	-	72.7
Relative density / %	30.3 ± 0.4	55.6 ± 4.4		92.3

Although the printed samples are still very porous, and structural integrity needs to be improved, the piezoelectric properties of KNN bodies obtained by binder jetting are promising according to the Figures of Merit (FoM) typically required of porous piezoceramics. Usually, porous piezoceramics are employed in the direct mode and the related FoM_{33} is calculated according to Eq. 2, as described in [36]:

$$FoM_{33} = d_{33}\, g_{33} \qquad (2)$$

It can be seen from the graph in Figure 9 that the printed samples subjected to the double sintering process feature an almost 100% improvement over the dense component obtained by traditional press-and-sinter technology. This is due to the proportionally larger increase of dielectric permittivity over d_{33} loss, as reported also by other studies [34,36,37].

Further investigation is needed to improve the mechanical and functional performances of these components, however it should be noted that the presented results already open the possibility of exploiting binder jetting for specific applications where porous piezoceramics may be advantageous over their dense counterpart [4,33,36,38].

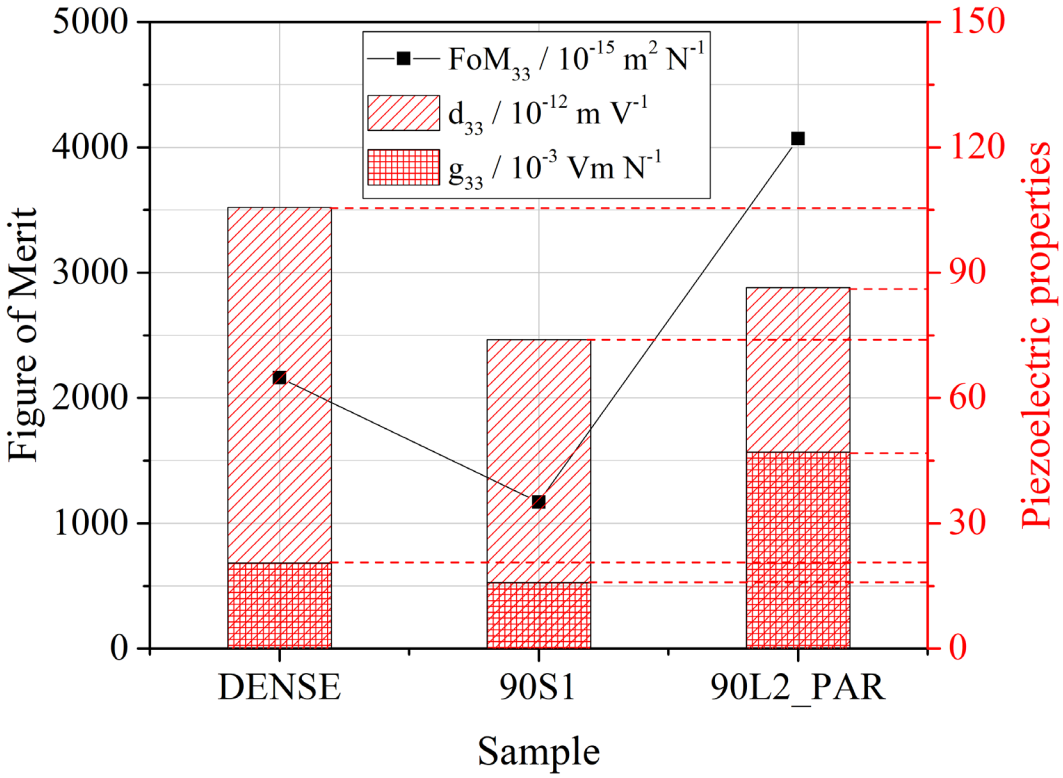

Figure 9 Comparison of the piezoelectric performance of the dense and porous samples.

In Figure 10 an example of very small samples with complex geometry that can be produced by binder jetting is shown; the morphology of the starting powders must be further optimised in order to improve the accuracy and the surface finishing.

Figure 10 Sintered KNN samples of complex geometry produced by binder jetting.

4. Conclusions

This study assesses the feasibility of producing KNN samples of complex geometry by binder jetting starting from as-synthesised powder; it exemplifies the possibility to adopt this additive manufacturing technique for the shaping of functional ceramics.

The powder packing behaviour and morphology of the green specimens demonstrate that even though raw materials still feature a poor flowability, relative density values above expectation may be achieved, thanks to the layer-by-layer deposition that reduces the risk of macropores formation within the powder bed. In this case, average green density values ranged in between ~30% and ~35%, depending on the binder saturation employed during printing, with at least a +5% improvement over tap density measured from rheometry.

Nevertheless, such low green compaction values prevented high densification and the sintering cycle needed to be doubled, with respect to die pressed samples, to achieve larger than 50% sintered density and sufficient mechanical integrity to allow safe handling of the

409 specimens. Micrographs parallel and perpendicular to the printing planes suggest porosity
410 anisotropy, which weakly affected the piezoelectric performances.
411 Finally, the increase of the Figure-of-Merit of the porous samples over the dense one paves
412 the way towards new applications of the binder jetting 3D printing technique in the area of
413 functional ceramics with complex shapes.
414
415

416 **Acknowledgements**

417 Authors would like to acknowledge the "Functional Sintered Materials (Funtasma)"
418 Interdepartmental Laboratory of Politecnico di Milano, where this research activity was
419 partially developed. Support by the Italian Ministry for Education, University and Research
420 through the project Department of Excellence LIS4.0 (Integrated Laboratory for Lightweight
421 e Smart Structures) is also acknowledged. EM and LC acknowledge the support from the
422 project "DIGIMAN – Soluzioni per la DIGItalizzazione delle aziende nel settore
423 MANifatturiero" – PG/2018/631166, in the frame of the POR FESR 2014-2020 programme
424 of the Regione Emilia Romagna (Italy).
425
426

427 **References**

428 [1] D. Huson, 3D printed ceramics: Current challenges and future potential, in: Int. Conf.
429 Digit. Print. Technol., 2016: pp. 374–377.
430 https://doi.org/https://www.ingentaconnect.com/content/ist/nipdf/2016/00002016/00
431 000001/art00094.
432 [2] Y. Zhang, L.M. Wu, X.Y. Guo, S. Kane, Y.F. Deng, Y.G. Jung, J.H. Lee, J. Zhang,
433 Additive Manufacturing of Metallic Materials: A Review, J. Mater. Eng. Perform. 27

(2018) 1–13. https://doi.org/10.1007/s11665-017-2747-y.

[3] Y. Lakhdar, C. Tuck, J. Binner, A. Terry, R. Goodridge, Additive manufacturing of advanced ceramic materials, Prog. Mater. Sci. 116 (2021) 100736. https://doi.org/10.1016/j.pmatsci.2020.100736.

[4] E. Mercadelli, C. Galassi, How to Make Porous Piezoelectrics? Review on Processing Strategies, IEEE Trans. Ultrason. Ferroelectr. Freq. Control. 68 (2021) 217–228. https://doi.org/10.1109/TUFFC.2020.3006248.

[5] C. Chen, X. Wang, Y. Wang, D. Yang, F. Yao, W. Zhang, B. Wang, G.A. Sewvandi, D. Yang, D. Hu, Additive Manufacturing of Piezoelectric Materials, Adv. Funct. Mater. 30 (2020) 2005141. https://doi.org/10.1002/adfm.202005141.

[6] European Parliament, Directive 2011/65/EU of the European Parliament and of the Council of 8 June 2011 on the restriction of the use of certain hazardous substances in electrical and electronic equipment (RoHS), Off. J. Eur. Union. 54 (2011) 88–110. https://eur-lex.europa.eu/legal-content/EN/TXT/?uri=CELEX%3A02011L0065-20210401 (accessed October 17, 2021).

[7] W. Chen, F. Wang, K. Yan, Y. Zhang, D. Wu, Micro-stereolithography of KNN-based lead-free piezoceramics, Ceram. Int. 45 (2019) 4880–4885. https://doi.org/10.1016/j.ceramint.2018.11.185.

[8] V. Sufiiarov, A. Kantyukov, A. Popovich, A. Sotov, Structure and properties of barium titanate lead-free piezoceramic manufactured by binder jetting process, Materials (Basel). 14 (2021) 4419. https://doi.org/10.3390/ma14164419.

[9] L.A. Chavez, P. Ibave, B. Wilburn, D. Alexander, C. Stewart, R. Wicker, Y. Lin, The

456 Influence of Printing Parameters, Post-Processing, and Testing Conditions on the
457 Properties of Binder Jetting Additive Manufactured Functional Ceramics, Ceramics.
458 3 (2020) 65–77. https://doi.org/10.3390/ceramics3010008.
459 [10] S.M. Gaytan, M.A. Cadena, H. Karim, D. Delfin, Y. Lin, D. Espalin, E. MacDonald,
460 R.B. Wicker, Fabrication of barium titanate by binder jetting additive manufacturing
461 technology, Ceram. Int. 41 (2015) 6610–6619.
462 https://doi.org/10.1016/j.ceramint.2015.01.108.
463 [11] A. Mostafaei, P. Rodriguez De Vecchis, I. Nettleship, M. Chmielus, Effect of powder
464 size distribution on densification and microstructural evolution of binder-jet 3D-
465 printed alloy 625, Mater. Des. 162 (2019) 375–383.
466 https://doi.org/10.1016/j.matdes.2018.11.051.
467 [12] S. Diener, A. Zocca, J. Günster, Literature Review: Methods for achieving high
468 powder bed densities in ceramic powder bed based additive manufacturing, Open
469 Ceram. 8 (2021) 100191. https://doi.org/10.1016/j.oceram.2021.100191.
470 [13] M. Mariani, R. Beltrami, P. Brusa, C. Galassi, R. Ardito, N. Lecis, 3D printing of fine
471 alumina powders by binder jetting, J. Eur. Ceram. Soc. 41 (2021) 5307–5315.
472 https://doi.org/10.1016/j.jeurceramsoc.2021.04.006.
473 [14] R. Beltrami, E. Mercadelli, C. Baldisserri, C. Galassi, F. Braghin, N. Lecis, Synthesis
474 of KNN powders: Scaling effect of the milling step, Powder Technol. 375 (2020) 101–
475 108. https://doi.org/10.1016/j.powtec.2020.07.098.
476 [15] M. Mariani, R. Beltrami, F. Meneghetti, D. Azzolini, N. Lecis, Effect of printing
477 parameters on the mechanical strength of green body from binder jetting additive

manufacturing, in: Procedia Eur. 2020 Int. Powder Met. Virtual Congr. Exhib., EPMA, 2020.

[16] B. Orayech, A. Faik, G.A. López, O. Fabelo, J.M. Igartua, Mode-crystallography analysis of the crystal structures and the low-and high-temperature phase transitions in Na0.5K0.5NbO3, J. Appl. Crystallogr. 48 (2015) 318–333. https://doi.org/10.1107/S1600576715000941.

[17] R.M. German, Prediction of sintered density for bimodal powder mixtures, Metall. Trans. A. 23 (1992) 1455–1465. https://doi.org/10.1007/BF02647329.

[18] W. Du, X. Ren, Y. Chen, C. Ma, M. Radovic, Z. Pei, Model guided mixing of ceramic powders with graded particle sizes in binder jetting additive manufacturing, ASME 2018 13th Int. Manuf. Sci. Eng. Conf. MSEC 2018. 1 (2018) 1–9. https://doi.org/10.1115/MSEC2018-6651.

[19] Y. Bai, G. Wagner, C.B. Williams, Effect of Particle Size Distribution on Powder Packing and Sintering in Binder Jetting Additive Manufacturing of Metals, J. Manuf. Sci. Eng. 139 (2017). https://doi.org/10.1115/1.4036640.

[20] M. Moghadasi, W. Du, M. Li, Z. Pei, C. Ma, Ceramic binder jetting additive manufacturing: Effects of particle size on feedstock powder and final part properties, Ceram. Int. 46 (2020) 16966–16972. https://doi.org/10.1016/j.ceramint.2020.03.280.

[21] A. Santomaso, P. Lazzaro, P. Canu, Powder flowability and density ratios: The impact of granules packing, Chem. Eng. Sci. 58 (2003) 2857–2874. https://doi.org/10.1016/S0009-2509(03)00137-4.

[22] R.B. Shah, M.A. Tawakkul, M.A. Khan, Comparative evaluation of flow for

pharmaceutical powders and granules, AAPS PharmSciTech. 9 (2008) 250–258. https://doi.org/10.1208/s12249-008-9046-8.

[23] Q. Li, V. Rudolph, B. Weigl, A. Earl, Interparticle van der Waals force in powder flowability and compactibility, Int. J. Pharm. 280 (2004) 77–93. https://doi.org/10.1016/j.ijpharm.2004.05.001.

[24] Y. Shiratori, A. Magrez, C. Pithan, Particle size effect on the crystal structure symmetry of K0.5 Na0.5NbO3, J. Eur. Ceram. Soc. 25 (2005) 2075–2079. https://doi.org/10.1016/j.jeurceramsoc.2005.03.012.

[25] T. Do, P. Kwon, C.S. Shin, Process development toward full-density stainless steel parts with binder jetting printing, Int. J. Mach. Tools Manuf. 121 (2017) 50–60. https://doi.org/10.1016/j.ijmachtools.2017.04.006.

[26] N. Lecis, M. Mariani, R. Beltrami, L. Emanuelli, R. Casati, M. Vedani, A. Molinari, Effects of process parameters, debinding and sintering on the microstructure of 316L stainless steel produced by binder jetting, Mater. Sci. Eng. A. 828 (2021) 142108. https://doi.org/10.1016/j.msea.2021.142108.

[27] Y. Mao, J. Li, W. Li, D. Cai, Q. Wei, Binder jetting additive manufacturing of 316L stainless-steel green parts with high strength and low binder content: Binder preparation and process optimization, J. Mater. Process. Technol. 291 (2021) 117020. https://doi.org/10.1016/j.jmatprotec.2020.117020.

[28] B. Malič, J. Koruza, J. Hreščak, J. Bernard, K. Wang, J.G. Fisher, A. Benčan, Sintering of lead-free piezoelectric sodium potassium niobate ceramics, Materials (Basel). 8 (2015) 8117–8146. https://doi.org/10.3390/ma8125449.

[29] H.C. Thong, C. Zhao, Z. Zhou, C.F. Wu, Y.X. Liu, Z.Z. Du, J.F. Li, W. Gong, K. Wang, Technology transfer of lead-free (K, Na)NbO3-based piezoelectric ceramics, Mater. Today. 29 (2019) 37–48. https://doi.org/10.1016/j.mattod.2019.04.016.

[30] M. Mariani, I. Goncharov, D. Mariani, G. Pietro De Gaudenzi, A. Popovich, N. Lecis, M. Vedani, Mechanical and microstructural characterization of WC-Co consolidated by binder jetting additive manufacturing, Int. J. Refract. Met. Hard Mater. 100 (2021) 105639. https://doi.org/10.1016/j.ijrmhm.2021.105639.

[31] D. Huber, L. Vogel, A. Fischer, The Effects of Sintering Temperature and Hold Time on Densification, Mechanical Properties and Microstructural Characteristics of Binder Jet 3D Printed 17-4 PH Stainless Steel, Addit. Manuf. 46 (2021) 102114. https://doi.org/10.1016/j.addma.2021.102114.

[32] H. Miyanaji, K.M. Rahman, M. Da, C.B. Williams, Effect of fine powder particles on quality of binder jetting parts, Addit. Manuf. 36 (2020) 101587. https://doi.org/10.1016/j.addma.2020.101587.

[33] P. Dixit, S. Seth, B. Rawal, B.P. Kumar, H.S. Panda, Freeze casting of lamellar-structured porous lead-free (Na0.52K0.48)(Nb0.95Sb0.05)O3 piezoceramic with remarkable enhancement in piezoelectric voltage constant and hydrostatic figure of merit, J. Mater. Sci. Mater. Electron. (2021) 1–11. https://doi.org/10.1007/s10854-021-05262-5.

[34] J.I. Roscow, H. Pearce, H. Khanbareh, S. Kar-Narayan, C.R. Bowen, Modified energy harvesting figures of merit for stress- and strain-driven piezoelectric systems, Eur. Phys. J. Spec. Top. 228 (2019) 1537–1554. https://doi.org/10.1140/epjst/e2019-

544 800143-7.

545 [35] L.A. Chavez, B.R. Wilburn, P. Ibave, L.C. Delfin, S. Vargas, H. Diaz, C. Fulgentes,
546 A. Renteria, J. Regis, Y. Liu, R.B. Wicker, Y. Lin, Fabrication and characterization of
547 3D printing induced orthotropic functional ceramics, Smart Mater. Struct. 28 (2019)
548 125007. https://doi.org/10.1088/1361-665x/ab4e0a.

549 [36] J. Roscow, Y. Zhang, J. Taylor, C.R. Bowen, Porous ferroelectrics for energy
550 harvesting applications, Eur. Phys. J. Spec. Top. 224 (2015) 2949–2966.
551 https://doi.org/10.1140/epjst/e2015-02600-y.

552 [37] Y. Zhang, M. Xie, J. Roscow, Y. Bao, K. Zhou, D. Zhang, C.R. Bowen, Enhanced
553 pyroelectric and piezoelectric properties of PZT with aligned porosity for energy
554 harvesting applications, J. Mater. Chem. A. 5 (2017) 6569–6580.
555 https://doi.org/10.1039/c7ta00967d.

556 [38] D.J. Shin, D.H. Lim, B.K. Koo, M.S. Kim, I.S. Kim, S.J. Jeong, Porous sandwich
557 structures based on BaZrTiO3–BaCaTiO3 ceramics for piezoelectric energy
558 harvesting, J. Alloys Compd. 831 (2020).
559 https://doi.org/10.1016/j.jallcom.2020.154792.

560